Halofilins as Emerging Bactofilin Families of Archaeal Cell Shape Plasticity Orchestrators

Zachary Curtis[1†], Pedro Escudeiro[2†], John Mallon[1†], Olivia Leland[1], Theopi Rados[1], Ashley Dodge[1], Katherine Andre[1], Jasmin Kwak[1], Kun Yun[3], Mechthild Pohlschroder[3], Vikram Alva[2]*, Alex Bisson[1]*

[1]Brandeis University, Department of Biology, Waltham, MA, USA
[2]Department of Protein Evolution, Max Planck Institute for Biology Tübingen, Tübingen 72076, Germany
[3]University of Pennsylvania, Department of Biology, Philadelphia, PA 19104, USA

[†] These authors contributed equally to this work and share the first authorship

* Co-corresponding authors.

Correspondence should be addressed to bisson@brandeis.edu

Author Contributions: AB, VA, MP, ZC, PE, and JM designed research; ZC, PE, JM, TR, OL, AD, KA, JK, and KY performed research; ZC, JM, OL, JK, KY and MP contributed new reagents/analytic tools; ZC, PE, JM, TR, OL, AD, and KY analyzed data; all authors contributed to the manuscript writing and revision.

Competing Interest Statement: The authors declare no competing interest.

Classification: Biological Sciences

Subgroup: Cell Biology

Keywords: Archaea; Shape Plasticity; Cytoskeleton; Structural Evolution; Bactofilin

Abstract

Bactofilins are rigid, non-polar bacterial cytoskeletal filaments that link cellular processes to specific curvatures of the cytoplasmic membrane. Although homologs of bactofilins have been identified in archaea and eukaryotes, functional studies have remained confined to bacterial systems. Here, we characterized representatives of two families of archaeal bactofilins from the pleomorphic archaeon *Haloferax volcanii*, halofilin A (HalA) and halofilin B (HalB). Unlike bacterial bactofilins, HalA polymerizes into polar filaments in vivo at positive membrane curvature, whereas HalB forms more static foci and accumulates in areas of local negative curvatures on the outer cell surface. Combining gene deletions, super-resolution, and single-cell microscopy showed that halofilins are critical in maintaining *H. volcanii* cell integrity during shape transition from disk (sessile) to rod (motile). Morphological defects in Δ*halA* primarily affected rod-shaped cells from accumulating highly positive curvatures. Conversely, disk-shaped cells were exclusively affected by *halB* deletion, showing a decrease in positive and negative curvatures, resulting in flatter cells. Furthermore, while Δ*halA* and Δ*halB* cells displayed lower cell division placement precision, morphological defects arose predominantly during the disk-to-rod shape remodeling. We propose halofilins provide mechanical scaffolding, dynamically coupling the cytoplasmic membrane and the S-layer. We speculate that HalA filaments support rods under low S-layer lipidation (flexible, fast membrane diffusion). In contrast, HalB connects the S-layer to negative curvatures in disks under high lipidation levels (rigid, slow membrane diffusion).

Significance Statement

How have cells evolved molecular machineries to support the mechanical and morphological requirements of microbial behavior? The biochemistry and biophysics of cell envelopes and their associated cytoskeleton are key to understanding such adaptations. Archaea are strategically positioned in the Tree of Life, bridging the molecular and cellular biology of bacteria and eukaryotes. Our work investigated the archaeal shapeshift between two morphological cell types and the role of two new cytoskeletal proteins in mechanical scaffolding during development. Specifically, halofilins are the first identified archaeal cell shape factors to be demonstrated to function at the onset of cell-type shifting. Broadly, our model offers potential for new synthetic cell designs and bioinspired materials that are both minimalist and modular.

Main Text

Introduction

Cell shape maintenance is as much of a universal trait as it is a focus of interest in every studied organism (1, 2). Cells employ diverse strategies to achieve shape control, like modulating the composition of the cell wall and the biophysical and biochemical properties of the cytoskeletal polymers that direct their organization (3–5). However, little is known about such mechanisms in Archaea, where cells lack a rigid, three-dimensional cell wall (6). Instead, the archaeal outer surface of the cytoplasmic membrane is coated by the S-layer, a lattice structure composed of glycoproteins (7, 8). Although the S-layer lattice is assembled through lateral, non-covalent protein interactions, the S-layer glycoprotein (SLG) can be covalently anchored to the cytoplasmic membrane by lipidation in some archaea (9, 10). Ultimately, the S-layer serves as a spatiotemporal reference for the biogenesis of appendage structures, such as pili and archaella (8). Still, its role as ruling cell shape biogenesis remains a topic of debate (11–13).

Haloarchaea are a class of salt-loving microbes notable for their vast morphological diversity, including rods, cocci, triangular, square, and other polygonal-shaped cells (14). Furthermore, the model organism *Haloferax volcanii* has been shown to reversibly shape-shift between two developmental states: the motile, rod-shaped cells and the sessile, polygonal disk-shaped cells (15–17). Mutations in the archaeosortase ArtA, required for the lipidation of SLG, resulted in an imbalance in the rod and disk equilibrium, favoring rod-shaped cell formation (9). Moreover, many *H. volcanii* cell-shape factors have been identified and characterized recently, with cytoskeletal polymers and associated proteins playing a central role. Among them, the tubulin-like paralogs FtsZ1 and FtsZ2 assemble the cytokinetic ring (Z-ring) and couple cell division with shape (18). Another superfamily of tubulin homologs, the CetZ proteins, direct rod-shape formation and motility (16). In contrast, the actin homolog, volactin, is required for the morphogenesis and viability of disk-shaped cells (19).

Bactofilins are a class of widely distributed bacterial cytoskeletal polymers with a conserved subdomain featuring a right-handed β-helical fold with highly variable N- and C-terminal ends (20, 21). Unlike most cytoskeletal proteins such as actin and tubulin, bactofilins spontaneously self-assemble into non-polar filaments independent of nucleotides and other cofactors (22, 23). *In vitro* studies have shown bactofilin polymers to be mechanically stable and resistant to high salt conditions and chelating agents (22). Their natural membrane affinity and rigidity are crucial for securing the recruitment of associated enzymatic complexes at specific subcellular locales (24, 25). Furthermore, bactofilin filaments have been characterized in many different species, playing essential roles in a multitude of cellular processes, including cell shape and stalk maintenance (25–29), chromosome segregation (30), and cell polarity (31).

Until recently, Bactofilins were considered exclusive to bacteria. However, recent work by Deng and colleagues has expanded the bactofilin universe to eukaryotes and archaea (23). Here, we use computational structural prediction, reverse genetics, and single-cell microscopy to characterize the evolutionary organization and *in vivo* function of two new archaeal bactofilins, halofilin A (HalA) and halofilin B (HalB) in the halophile *H. volcanii*.

Results

Halofilins represent diverse families of the bactofilin superfamily

A sequence search for bactofilin homologs in the archaeal model *H. volcanii*, using the Pfam bactofilin domain (PF04519) as query, yielded two previously reported candidates, now designated halofilin A (HVO_1610 / UniProtKB D4GZ39) and halofilin B (HVO_1237 / UniProtKB D4GX31). Subsequent analysis of the structures predicted by AlphaFold2 (32) revealed that HalA consists of two bactofilin-like domains arranged head-to-head and connected by an alpha-helical

hairpin (between residues Arg122 and Asp161). The N- and C-termini of HalA exhibit disordered tails (Fig. 1A), a feature also common in bactofilins. Each bactofilin subdomain in HalA has six right-handed windings of parallel beta-strands that form a single-stranded, three-faced, right-handed beta-helix, equivalent to canonical bactofilins. Notably, the N- and C-terminal bactofilin subdomains of HalA superimpose at a root-mean-square deviation (RMSD) of ~1 Å and superimpose with *Thermus thermophilus* bactofilin (TtBac) at RMSDs of ~2 Å and ~1.6 Å, respectively. To identify potential polymerization interfaces of HalA, we used AlphaFold2-Multimer (32, 33) to generate homodimer predictions. In most of these models, the HalA monomers are arranged C-terminus-to-C-terminus, with no cases of N-terminus-to-N-terminus observed (Fig. S1A-D). Interestingly, in one of the top-ranking models, the dimerization interface is formed by the alpha-helical hairpins (Fig. S1E). The first alpha-helix of the hairpin motif is enriched in hydrophobic amino acids (Fig. S1F) and could also serve as a membrane-targeting sequence (MTS). We also attempted to predict structures for homotrimers and homotetramers of HalA using AlphaFold2-Multimer; however, these predictions yielded inconclusive results. As a control, we used AlphaFold2-Multimer to predict homo-oligomers of TtBac, obtaining filaments with subunits arranged in a head-to-head configuration, which is in agreement with the solved TtBac filament structure.

Unlike HalA, HalB is predicted to be an alpha-helical integral membrane protein with a predicted Sec/SPI signal peptide and five transmembrane (TM) helices. A sixth, shorter helix is positioned parallel to the inner leaflet of the membrane (Fig. 1B). In addition, HalB has an extracellular bactofilin domain with five windings at its N-terminus (residues 41-125, henceforth denoted as bHalB), contrasting the six found in HalA and TtBac, and possesses a disordered cytoplasmic tail at its C-terminus. The bactofilin domain of HalB superimposes with the bactofilin subdomains of HalA at RMSDs of ~2 Å and with TtBac at ~1.5 Å. Notably, AlphaFold2-Multimer models for homo-oligomers of bHalB also did not yield conclusive oligomers.

To systematically assess the relationship between HalA, HalB, and canonical bactofilins at the sequence level, we performed pairwise BLASTp comparisons of (i) HalA and TtBac, (ii) bHalB and TtBac, and (iii) HalA and bHalB. The C-terminal bactofilin subdomain of HalA (residues 180-259) shows apparent homology to TtBac (identity = 29.79%, query coverage = 72%, E-value = 5e-6, Fig. S2A), whereas the N-terminal subdomain aligns only partially and with very low significance (E-value = 0.47) to TtBac. To further investigate the evolutionary relationship between the N-terminal bactofilin subdomain of HalA and canonical bactofilins, we used the sensitive remote homology detection method HHpred, which is based on profile Hidden Markov Models (HMMs) [ref]. Through this analysis, we found a statistically significant match between the N-terminal subdomain of HalA (residues 12-114) and the Pfam bactofilin domain PF04519 (Pr = 89.39%, E-value = 0.043). These results indicate that the N-terminal subdomain shows greater divergence from canonical bactofilins compared to the C-terminal subdomain. BLASTp found no statistically significant similarity between bHalB and either TtBac or HalA. However, using HHpred, we obtained statistically significant matches between bHalB and TtBac (Pr = 98.53%, E-value = 1.8e-15) and between bHalB and the C-terminal bactofilin subdomain of HalA (Pr = 93.76%, E-value = 1.8e-7), suggesting that bHalB is also homologous to bactofilins.

To further substantiate the observed sequence relationship between HalA, HalB, and bactofilins on a global scale, we assembled their homologs from UniProtKB and clustered them using CLANS (34) based on the strength of their all-against-all pairwise sequence similarities (see Methods for details). In the resulting cluster map, HalA, HalB, and bactofilin sequences are organized into three distinct clusters (Fig. 1C). At the E-value cut-off (1e-8) chosen to visualize the connections, the HalA and HalB clusters are connected to the bactofilin cluster but not to each other, indicating a closer relationship between HalA and bactofilins. Eukaryotic bactofilins, found in stramenopiles and ascomycetes and exemplified in the cluster map by the stramenopile *Phytophthora infestans* bactofilin PiBac, cluster tightly together with canonical bacterial bactofilins. This supports the hypothesis that these eukaryotes may have acquired bactofilins

from bacteria by horizontal transfer, as previously proposed (23). Besides the HalA, HalB, and bactofilin assemblages, our map contains a fourth, smaller group radiating from the bactofilin cluster (BacEF). This cluster consists of bacterial and archaeal bactofilin-like proteins with 13 windings, represented by homologs of BacEF (UniProtKB P39132 and P39133) from *Bacillus subtilis* (24, 35) and the uncharacterized protein from *Methanobacterium bryantii* (UniProtKB A0A2A2H537).

The HalA cluster consists of proteins (n = 681) exclusively from Archaea (Fig. S2), with most homologs originating from the phylum Euryarchaeota, in particular from Halobacteria (n = 382) and Methanomicrobia (n = 192). Additionally, we found some homologs in archaeal candidates and unclassified phyla, including the Asgard group. Analysis of AlphaFold2-predicted structures for numerous HalA sequences revealed that although they share a head-to-head stacked fold, an equal number of windings in each bactofilin subdomain, and the alpha-helical hairpin, they exhibit great diversity in their N- and C-terminal alpha-helices and disordered tails (Fig. S4). In contrast, the HalB cluster (n = 2,304) shows a broader distribution across both archaea and bacteria, with a higher prevalence (n = 1,813) in the latter (Fig. S3). Akin to HalA, archaeal HalB is predominantly found in Euryarchaeota (n = 454), especially in Halobacteria (n = 280) and Methanomicrobia (n = 152). Within Bacteria, HalB is most abundant in Chloroflexota (n = 387), Pseudomonadota (n = 287), and Bacillota (n = 170). Additionally, HalB is found in numerous unclassified clades, candidate phyla, and divisions of both Bacteria and Archaea. HalB variants also exhibit broader structural diversity (Fig. S4). For example, the bHalB domains comprise up to ten windings among all the analyzed structures. The C-terminal tail also shows significant variability; in some cases, it is associated with an additional domain and may extend further into the cytoplasm (e.g., A0A3B9P870), while in others it is absent (e.g., A0A662QX32). Nonetheless, all HalB homologs have a TM domain with the same number of alpha-helices preceded by an unstructured segment.

The widespread taxonomic distribution of bactofilins across the three domains of life suggests that a primordial form of these proteins may have existed at the time of the last universal common ancestor (LUCA). It is likely that HalA originated from the duplication, fusion, and subsequent diversification of an ancestral bactofilin-like gene. Similarly, HalB might have arisen by the fusion of an ancestral bactofilin-like gene with one encoding a TM domain, followed by diversification (Fig. S4). Notably, HalA and HalB are predominantly found in the Halobacteria and Methanomicrobia classes (Figs. S2 and S3), indicating the possibility of an underlying co-evolutionary relationship between these proteins.

HalA and HalB show different localization and dynamics in vivo

To determine whether HalA and HalB polymerize in their native cellular environment, as expected for a bactofilin cytoskeleton, we created cells expressing C-terminal msfGFP fusions as a second copy. Imaging cells using epifluorescence microscopy, HalA-msfGFP was found to assemble into relatively long filaments with no specific subcellular localization (Fig. 2A, top left panel). Super-resolution 3D projections from SoRa spinning-disk confocal images revealed curved HalA filaments on the inner surface of the cytoplasmic membrane (Fig. 2A, top right panel, Movie S 1). In contrast, HalB-msfGFP organizes as bright foci distributed around the cell's contour (Fig. 2A, bottom panels, Movie S1). Interestingly, we did not observe HalB-msfGFP forming pronounced polymer structures akin to HalA-msfGFP. However, we cannot exclude the possibility that HalB still polymerizes into subdiffractional filaments.

Next, we collected time lapses with epifluorescence across multiple generations to assess whether HalA and HalB structures are dynamically regulated throughout the cell cycle. Like BacEF bactofilins that orchestrate flagella location (24, 35), HalB foci show slow diffusion across the membrane (Fig. 2D, Movie S2). Conversely, HalA filaments are unusually more dynamic than the studied bactofilins, exhibiting polar polymerization and depolymerization at a rate 10-fold faster than the cell cycle period (Fig. 2B, Movie S3). Nonetheless, HalA filaments often persist in

their cellular locales for extended periods, with depolymerization occurring twice as fast as polymerization rates (Fig. 2C). Therefore, polar HalA filaments might have substantial differences in their polymerization mechanism compared to known non-polar bactofilins.

The MTS and the C-terminal subdomain are required for HalA polymerization

To further understand the structural principles underlying HalA polymerization, we created a series of truncated HalA-msfGFP constructs and tested whether they could perturb HalA filaments tagged with HaloTag. While HaloTag technology has been widely employed *in vivo* across many bacteria and in the haloarchaeon *Halobacterium salinarum* (36), some microbes, such as fission and budding yeast, require transporter deletions to retain the dyes in the cell (37, 38). To validate the HaloTag in *H. volcanii*, we incubated cells expressing cytoplasmic HaloTag with a mix of the probes JF549 (permeable) and Alexa488 (non-permeating) HaloTag ligands. Consequently, we observed a cytoplasmic HaloTag-JF549 signal but not Alexa488 (Fig. S5, top row). As a control, we also incubated wild-type cells (without HaloTag expression) and observed no significant labeling with either JF549 or Alexa488 HaloTag ligands (Fig. S5, bottom row). Based on these observations, we concluded that HaloTag is a proper reporter for specific protein labeling in live *H. volcanii* cells.

Since HalA-HaloTag assembled into polymers like HalA-msfGFP (Fig. 3A, top-left panel), we proceeded to test if the co-expression of the selected constructs perturbed the polymerization of HalA. First, we tested whether the MTS region is required for HalA polymerization. Therefore, we replaced the MTS (R122-Asp161) with a 40aa-long flexible linker (ΔMTS::40aa). Expression of HalA lacking MTS extensively depolymerized the HalA filaments, suggesting that the HalA(ΔMTS::40aa) can still be incorporated into polymers but with decreased affinity for the membrane (Fig. 3A, top-center panel). A non-mutually exclusive hypothesis is that the MTS sequences may be involved in the polymerization contact of HalA filaments (Fig. S1E and S1G), which could explain the polar dynamics seen in our time lapses. To probe the MTS interaction with the HalA polymers, we expressed HalA(MTS) alone, positioned between msfGFP and mYPet fluorescent proteins. Analogous to the HalA(ΔMTS::40aa) construct, the MTS was sufficient to depolymerize HalA, suggesting that the alpha-helical hairpin may be involved in more than just HalA membrane anchoring (Fig. 3A, top-right panel).

Next, we investigated the role of the N-terminal and C-terminal ends of HalA and whether they are, as in canonical bactofilins, part of the polymerization surface. For this purpose, we expressed the N-terminal subdomain (1-170aa) and observed extensive depolymerization of HalA (Fig. 3A, bottom-left panel). However, this region encompasses the MTS, which alone can depolymerize HalA. Hence, we created an N-terminal subdomain in which the MTS region was replaced with a 40aa flexible linker. This time, unlike bacterial bactofilins, the N-terminal subdomain lacking the MTS was insufficient to depolymerize HalA filaments (Fig. 3A, bottom-center panel). Finally, the expression of the C-terminal subdomain alone induced depolymerization of HalA (Fig. 3A, bottom-right panel). Altogether, these results suggest that the MTS and C-terminal regions, but not the N-terminus, play a role in the polymerization, membrane interaction, and/or stability of HalA filaments.

bHalB bactofilin subdomain is located at the extracellular surface

HalB represents the first multipass transmembrane protein with its bactofilin domain predicted to be cell-surface exposed, distinguishing it from other bactofilins that are cytoplasmic. To validate our model of HalB membrane topology, we again explored the (non)permeability of Alexa488 and JF549 to cell membranes. To test the HalB topology, we created two new HalB-HaloTag constructs: one mimicking the predicted cytoplasmic C-terminal msfGFP fusion shown in Figure 2, and the second a sandwich fusion inserting HaloTag adjacent to the Ser34 residue between the predicted Sec secretion signal (residues 1-30) and the bHalB subdomain (Fig. 3B). As expected, both HalB-HaloTag constructs were labeled with the cell-permeable JF549, while Alexa488 specifically decorated the extracellular HaloTag fusion (Fig. 3C). From the localization,

dynamics, and topology profile, we conclude that HalB is a transmembrane protein whose bactofilin domain is exposed to the outer cell surface, linked by a flexible linker long enough to be placed towards the S-layer plane (39).

Halofilin mutants show modest but significant defects in growth, viability, and motility

To investigate the function of halofilins, we created strain deletions of *halA*, *halB,* and the double mutant Δ*halAB*. We started by characterizing standard microbiological phenotypes: growth, viability, and motility. Despite not observing severe defects in bulk growth between the wild type and the mutants (Fig. S6A), Δ*halA* and Δ*halAB* showed a significant decrease in viability (64±30% and 65±30% of the wild type, respectively) and motility (49±9% and 36±5% of the wild type, respectively) (Fig. S6B-C). Interestingly, Δ*halB* showed no viability decrease and only a subtle decrease in motility (91±9% and 79±10% of the wild type, respectively). These results suggest that HalA and HalB may have non-redundant functions.

Δ*halA *and Δ*halB *are transiently dominant-negative in different cell types

The phenotypes of halofilin mutants include confounding factors due to physiological differences in *H. volcanii* cells under different growth stages. Many haloarchaeal species show developmental shape transitions between disks (pili-based, sessile cells) and rods (archaella-based swimming cells). Shape transitions have been shown to occur across bulk growth phases, with a majority of rods or disks found in the early-exponential and mid-exponential phases, respectively (15, 17). Consequently, the motility defects of halofilin mutants could be related to rod shape.

To determine whether each halofilin functions in different cell types, we initially imaged cultures with mixed populations of rods and disks using live-cell 3D-SoRa super-resolution (Fig. 4A, Movie S4), combined with phase contrast microscopy (Fig. S7A). The deletion of *halA* resulted in elongated, irregular rods, but disks remained relatively typical (Fig. 4B, S7B). However, Δ*halB* rods were only mildly misshapen, and disks appeared larger and more angular than the wild type. Moreover, rods of the Δ*halAB* double mutant showed a solidity profile similar to that of Δ*halA*. Nonetheless, Δ*halAB* cells displayed comparable disk-shape defects as observed in Δ*halB*. Therefore, the rod-related morphology phenotypes in Δ*halA* and Δ*halAB* match with the motility deficiencies (Fig. S6C). These results suggest that HalA and HalB perform non-overlapping functions, potentially becoming relevant in different lifestyles of *H. volcanii* cells.

Halofilin deletions show distinct envelope curvature profiles

Previous work on *Helicobacter pylori* has shown that the bactofilin CcmA counterbalances MreB-directed cell wall synthesis to enforce helical curvature (40). Since Δ*halA* and Δ*halB* distinctively impact rod- and disk-cell morphologies, we tested whether halofilins can regulate cell envelope curvature. First, we used our 3D-SoRa dataset of mutant cells (Fig. 4A, Movie S4) to extract submicron membrane curvature maps from wild type and each halofilin mutant (Fig. 5A). The Gaussian curvature distributions showed a predominance (>50%) of neutral Gaussian curvatures in both rods and disks. To visualize subtle but crucial differences in our samples, we curated our datasets and selected only the top 25 percentile of both negative and positive curvatures from each dataset.

As a result, we found that the mutant rods showed only slight differences in negative curvatures across Δ*halA*, Δ*halB,* and Δ*halAB* strains, observed only below the tenth percentile (Fig. 5B, top- and bottom-left panels). However, Δ*halA* and Δ*halAB* rods were pronouncedly shifted towards positive curvatures ($\mu_{1/2}$=12.5±1.7 and 14.3±1.9μm^{-2}, respectively) compared to wild type ($\mu_{1/2}$=8.8±0.9μm^{-2}). In contrast, the positive curvatures of the Δ*halB* rod cells were again alike the wild type (Fig. 5B, top-right panel). This negative-dominant effect of Δ*halA* over Δ*halAB* rods corroborates the cell shape measurements shown in Figure 4B. Nevertheless, the disk curvature distributions revealed a recurring pattern of dominance reversal: Δ*halA* cells approximated the wild type distribution, while Δ*halB* and Δ*halAB* skewed from extreme positive curvatures to flatter

surfaces ($\mu_{1/2}$=3.6±0.5 and 3.8±0.9µm-2, respectively), compared to wild type ($\mu_{1/2}$=6.1±0.6µm-2) (Fig. 5B, bottom panels).

HalA and HalB bind to specific membrane curvatures

Since disk and rod curvatures rely on each halofilin differently (Fig. 5B), and because we did not observe HalA filaments or HalB foci being recruited to specific subcellular locations (Fig. 2A), we hypothesized that HalA and HalB should have an affinity for specific membrane curvatures. Hence, HalA must be capable of localizing to specific regions to prevent the increase of extreme positive curvatures (above 10µm^{-2}) in rods. In contrast, HalB maintains the balance of negative and positive curvatures, preventing them from becoming flatter. Therefore, we revisited our 3D-SoRa dataset of cells expressing HalA-msfGFP and HalB-msfGFP (Fig. 2A, Movie S1), obtaining curvature measurements mapped across XYZ positions and comparing them with the normalized intensity profile map of each halofilin fusion. Notably, both HalA-msfGFP and HalB-msfGFP showed a strong preference for positive and negative curvatures, respectively (Fig. 5C). However, their accumulation was more pronounced in rods (HalA) or disks (HalB), suggesting that their physical interaction, if it exists, should be transient in a fully developed cell type.

Although preferential localization to specific curvatures could facilitate proteins to engage in membrane remodeling, it is not sufficient to conclude that halofilins are actively involved in creating specific curvatures in the cell. To test if halofilins could individually deform cells, we overexpressed HalA and HalB with the robust and inducible promoter Pxyl (41). Cultures overexpressing HalA (*halA* OE) under the microscope showed very few (but relatively standard) rods compared to wild type and Δ*halA*. Meanwhile, most of the disk populations comprised larger, deformed cells (Figs. 5D and S8, Movie S4). Furthermore, while we qualitatively observed more rod-like cells under HalB overexpression, they were more deformed than the fewer ones seen in the *halA* OE sample. Finally, we observed a similar size and shape profile in *halB* OE disk cells compared to *halA* OE. These results support our hypothesis that HalA and HalB are required for maintaining proper cell curvature balance by scaffolding the membrane at vulnerable positive and negative curved submicron locales.

Membrane curvature influences cell division placement

Based on the morphological defects observed at the cell poles of halofilin mutant cells (Fig. 4A), we sought to investigate whether HalA and HalB can influence cell division. Most archaea assemble their cell division machinery by assembling the Z-ring with two tubulin-like cytoskeletal filaments, FtsZ1 and FtsZ2. Recently, Liao et al. proposed that each FtsZ paralog might play non-overlapping roles, such as FtsZ1 in cell elongation/shape and FtsZ2 in cytokinesis (18). To probe the Z-ring localization in the halofilins mutants, we expressed FtsZ1-GFP and FtsZ2-GFP in the background of each mutant strain and imaged rod and disk cell populations (Figs. 6A and S9A-B). We found that Z-rings decorated with either FtsZ1-GFP or FtsZ2-GFP showed greater positional variance across the long axis of the halofilin mutant rod cells, with a more pronounced decondensation of Z-rings in the Δ*halA* and Δ*halAB* mutants (Fig. 6B, S9A). However, we did not observe as drastic a decondensation of the Z-ring in the disk-shaped mutants (Fig. S8B).

Although Z-ring condensation is required for bacterial survival (42, 43) and may explain why rod-shaped Δ*halA* and Δ*halAB* mutants have a larger cell area, cell division defects alone cannot explain the Δ*halB* and Δ*halAB* phenotype in disks. It is often challenging to decouple morphological defects caused by cell division from cell-shape defects that cause pleiotropic cell division defects (44, 45). To investigate each scenario, we correlated the position of the Z-ring with the area of each single-cell rod from our consolidated FtsZ1-GFP and FtsZ2-GFP datasets. The expectation is that if Z-ring position/condensation is directly responsible for the emergence of cell shape defects, we should observe an early delocalization of Z-rings that precedes an increase in cell area. Consequently, we would find only a weak correlation between cell area and Z-ring position. However, if the cells are initially misshapen and then increase in size, cell division would be a side effect and the Z-rings would therefore only delocalize in larger rods. In

agreement with the latter hypothesis, Z-ring positions deviated most from the midcell position in rods with larger cell areas. In contrast, halofilin mutants with average cell size showed an indistinguishable Z-ring position from the wild type (Fig. 6C).

However, the cell area of halofilin mutants may not be the best predictor of cell shape, as cells can be larger and have indistinguishable solidities from the wild type. To directly observe the relationship between cell shape defects and division, we tested whether solidity defects observed in Δ*halA* (rods) and Δ*halB* (disks) emerged during cytokinesis, which should be driven by FtsZ2 decondensation. Therefore, we tracked the solidity of healthy single cells from the onset of constriction to complete daughter cell separation. We expected to observe a drastic drop in cell solidity during cytokinesis, which should recover in a fast, one-step phase upon daughter cell split. If cell constriction creates misshapen cells, we should see cells failing to recover their solidity to initial levels. Conversely, we observed that the Δ*halA* and Δ*halB* mutants recovered their solidity to a similar level as the wild type (Figs. 6D and S9C, Movie S5). Interestingly, the Δ*halA* rods showed a steeper increase in solidity than the wild type and Δ*halB*, although the cells recovered solidity levels above 0.9.

Finally, we tested if the delocalization of FtsZ1 in halofilin mutant cells could contribute to cell shape defects by affecting the elongation and lipidation of the S-layer (9, 18). By tracking the solidity of healthy Δ*halA* and Δ*halB* cells, we did not observe cell shape defects beyond those seen in the wild type (Figs. 6E and S9D, Movie S5). Combining both analyses, we conclude that halofilins are not directly involved in shape maintenance during cell division and elongation.

Halofilins mechanically protect cells during disk-to-rod shape transitions

Most of the haloarchaeal cell shape factors identified in recent years play a role in stabilizing cell-type morphologies by shifting the apparent ratio of cell shapes across populations to be dominated by rods or disks (9, 16, 19). However, it is not evident whether these regulators play a specific role during shape transitions. Since halofilin mutants still form rods and disks, albeit with partial, cell-type specific defects, we propose that they play a role during the shape transition process.

Among other technical challenges, the study of mechanistic details during shape transitions has so far been limited by the ability to observe the cells shifting under the microscope in real time. Therefore, we developed a protocol to increase the frequency of multiple simultaneous shape transitions, establishing an easy and affordable assay to quantify time and morphology integrity during transitions. Because cells from isolated colonies on plates are mostly disk-shaped and rods emerge very early in exponential growth in liquid, we speculated that these disks from plates should shape-shift in liquid culture as soon as they leave the lag phase. Hence, we streaked fresh plates until colonies were barely visible, resuspended them in liquid media, and moved samples directly to the microscope. As expected, cells started to transition approximately one generation after resumption of growth.

Next, we tracked the solidity of cells shifting from disks to rods. Following the same logic as in the cell division assay, bactofilin mutants should deform during disk-to-rod shape transitions beyond the wild-type control. For tracking, we selected only disk cells with a standard cell shape (solidity>0.95). While wild-type disks transitioned smoothly to rods with mean solidities of approximately 0.95 (Fig. 6F-G, Movie S6), Δ*halA* cells abruptly deformed only during the second half of the transition period, resulting in rods with mean solidities of approximately 0.85. Meanwhile, Δ*halB* cells followed the same trend as Δ*halA*, but with an early solidity decay in the first half of the process, followed by a subtle recovery to mean solidities of approximately 0.93. In summary, halofilin mutants result in more drastic cell shape defects compared to our previous bulk measurements. This suggests that cells rely on halofilins for mechanical support during disk-to-rod shape remodeling, with HalB preventing deformations in the first phase of the process

when the cells are still disks. Later, HalA plays a role in the second phase, when the cells have almost fully developed into complete rods.

Discussion

Although most microbes regulate cell shape by patterning the cell wall, it is unclear whether archaeal cells control morphogenesis through the turnover of the S-layer lattice or, analogous to eukaryotic cell-wall-less cells, through invoking an additional layer of mechanical scaffolding from cytoskeletal polymers. Eukaryotic cytoskeleton systems often fulfill multiple functions, such as cargo transport, mechanosensing, and scaffolding (46, 47). Meanwhile, bacterial polymers could be classified as "cytomotive", dynamically localizing synthases to build, for example, organized cell wall structures, thereby playing the role of an exoskeleton by mechanically supporting cell shape (48–50). Distinguishing between these two models is particularly relevant for cells undergoing shape transitions, such as *H. volcanii*. Cell-walled cells have evolved the ability to confine higher intracellular pressure, albeit at the cost of having to slowly build (over many generations) *de novo* cell walls during morphological recovery or development (51, 52). However, disk-to-rod shape transitions in *H. volcanii* occur within a quarter of its generation time (Fig. 6F). One interpretation is that the turnover of the S-layer lattice and/or the conformation changes of the SLG protein facilitate a faster reshaping of the cell envelope. Hence, archaeal cells could combine a hybrid approach using cytomotive and cytoskeletal polymers, including halofilins, to provide structural support during morphogenesis.

By probing the function of the halofilins HalA and HalB, we have drawn a parallel to canonical bactofilins, such as a preference for specific membrane curvatures to prevent cells from warping at critical regions (Fig. 5C). Moreover, *halB* deletion in disk-shaped cells resulted in trends resembling those in the spiral-shaped bacterium *H. pylori*, where defects in the bactofilin CcmA led to the flattening of membrane curvatures (26, 40). However, the similarities ceased when Δ*halA* rod-shaped cells showed a shift to positive curvatures (Fig. 5B). While we can speculate that HalA's preference for positive curvatures may be due to its potential to form a polymer arc, there is currently no evidence to suggest that HalB forms polymers (Fig. 2). Nevertheless, there are numerous examples of transmembrane proteins that bind to and enforce specific membrane curvatures. For instance, the nicotinic acetylcholine receptor oligomerizes into conical structures that stabilize membrane folds at the neuromuscular junction (53). It is possible that HalB supports positive curvatures by creating limited diffusion barriers through interactions with the S-layer, assisting HalA filaments to localize at specific sites (Fig. 7).

The peculiarities of HalA are not limited to its structural features, but also extend to its dynamics in cells. Unexpectedly, HalA filaments showed directional polymerization and depolymerization reminiscent of nucleotide-binding cytoskeletons, in contrast to canonical bactofilins and other non-polar filaments such as intermediate filaments (54). One possible explanation is that the MTS not only recruits HalA filaments to the membrane but also interacts with itself to confer polymerization directionality (Fig. 2B). Two sets of observations support this view: 1) the depolymerization rate of HalA filaments is twice as fast as directional polymerization (Fig. 2C), suggesting that there are at least two polymerization surfaces or two conformational states; 2) the inability of the HalA N-terminal subdomain to depolymerize HalA filaments (Fig. 3A), suggesting that this surface is not involved in polymerization. However, it is also possible that our truncated mutant is inactive because it does not fold correctly by itself. Alternatively, HalA polymerization/depolymerization could also be induced by the interaction with other (possibly) polar cytoskeletons in the membrane, such as volactin (19), FtsZs (18), and CetZs (16). Lastly, another possible mechanism could mimic the major sperm protein (MSP) filament, a non-polar cytoskeleton that shows polymerization directionality induced by end-tracking motors to confer directionality to nematode sperms (55). In any scenario, achieving polymer polarity requires a

structural switch that modulates the affinity between monomers and subunits of the filament (56, 57).

The observation that the deletion of halofilins result in decondensation of the Z-ring at the midcell leaves open questions for the future (Fig. 6A). Even though the resulting defects are likely due to membrane curvature aberrations created during shape transitions, we can speculate that the spatiotemporal control of negative and positive curvatures across the cell could be an active form of positioning of the cell division machinery across different cell shapes. Implying that controlled membrane deformation plays an active role in Z-ring positioning aligns with the absence of a dedicated Min system in archaea (58) and aligns with mathematical models linking cell shape to Turing patterns (59). Moreover, this could expand our understanding of Z-ring positioning universally across bacteria, where cells direct cell division placement with high accuracy even without Min and nucleoid occlusion systems (60–62).

A central outstanding question in the field is how closely related haloarchaeal species build different cell shapes (14). Mutants disrupting the covalent attachment of the SLG protein to phospholipids showed an enrichment of rods and delaying the transition to disks to late exponential phase (9). This supports the hypothesis that the S-layer may have a lower degree of lipidation in rods than in disks, corroborating the higher proportion of negative and positive curvatures in rods. Disks, on the other hand, are flatter, possibly due to reduced membrane fluidity caused by the attachment to the S-layer lattice (Fig. 5B). Furthermore, little is known about the dynamics of the S-layer and how many SLG lattice conformations exist in rods and disks and during shapeshift between them (63). von Kügelgen and colleagues recently combined cryo-EM and *in situ* cryo-ET to show that the *H. volcanii* S-layer comprises SLG ensembles of symmetric P6 groups but with P5 groups in high curvature regions (39). Interestingly, the bHalB subdomain may be at the same plane as the S-layer, which could explain its static dynamics (Fig. 2D, Movie S2). Consequently, bHalB interaction with the S-layer could be mediating lattice reorganization in disks on the verge of shapeshift.

In summary, we propose a model of how halofilins contribute to disk-to-rod shape transitions at different, sequential stages (Fig. 7). At the beginning of the shape transition process, HalB induces lattice remodeling at negative membrane curvatures to counterbalance the rigidity of the membrane attached to the S-layer lattice. It is also possible that HalB directs the removal of lipidated SLG, promoting the turnover to the unlipidated lattice mostly present in rods. Thereafter, as the shifting cells decrease the levels of lipidation, HalA filaments dynamically accumulate at positive curvatures to prevent membrane Gaussian curvatures above $10\mu m^{-2}$. Therefore, when Δ*halB* disk cells fail to control S-layer remodeling in the first stage of development, HalA could partially repair cells by reinforcing positive curvatures. This might explain why we did not observe significant defects in Δ*halB* rods and Δ*halA* disks, the latter case is perhaps connected to rod-to-disk transitions. Future studies should elucidate the details of the possible interactions between HalA and HalB during shape transitions, and whether halofilin filaments scaffold the membrane directly or through the recruitment of S-layer factors like canonical bactofilins. Ultimately, the mechanistic details of how archaeal cytoskeleton will expand our understanding about the switch from cytomotive to multi-functional polymers after eukaryogenesis.

Materials and Methods

A detailed description of protocols, and reagents, as well data and software availability can be found in Supporting Information.

Acknowledgments

The authors thank Bruce Goode and Avital Rodal (Brandeis U) for their comments on our manuscript. The Bisson Lab appreciates the Goode Lab (Brandeis U) for access to their SoRa microscope. The authors are grateful to Benjamin Bratton (Vanderbilt U) and Thomas Fai (Brandeis U) for their advice on Gaussian Curvature analysis. This work was supported by the Moore–Simons Project on the Origin of the Eukaryotic Cell (doi:10.46714/735929LPI) awarded to AB; the Human Frontiers Science Program (RGY0074/2021) awarded to AB and VA; the National Science Foundation Grant (NSF-MBC2222076) awarded to MP and AB; and the Brandeis National Science Foundation (NSF) Materials Research Science and Engineering Center (MRSEC) Bioinspired Soft Materials (NSF-DMR 2011846). AB is a Pew Scholar in the Biomedical Sciences, supported by The Pew Charitable Trusts. This work was partly supported by institutional funds of the Max Planck Society. VA would like to thank Andrei Lupas (MPI Tübingen) for their continued support.

References

1. R. Gordon, M. M. Hanczyc, N. D. Denkov, M. A. Tiffany, S. K. Smoukov, Emergence of polygonal shapes in oil droplets and living cells: The potential role of tensegrity in the origin of life. *Habitability of the Universe before Earth* (2018).

2. J. A. THOMSON, On Growth and Form. *Nature* **100**, 21–22 (1917).

3. P. D. Caccamo, Y. V. Brun, The Molecular Basis of Noncanonical Bacterial Morphology. *Trends Microbiol* **26**, 191–208 (2018).

4. A. Sapala, *et al.*, Why plants make puzzle cells, and how their shape emerges. *eLife* **7**, e32794 (2018).

5. E. C. Garner, Toward a Mechanistic Understanding of Bacterial Rod Shape Formation and Regulation. *Annual Review of Cell and Developmental Biology* **37**, 1–21 (2021).

6. M. van Wolferen, A. A. Pulschen, B. Baum, S. Gribaldo, S.-V. Albers, The cell biology of archaea. *Nature Microbiology* **7**, 1744–1755 (2022).

7. T. Rodrigues-Oliveira, A. Belmok, D. Vasconcellos, B. Schuster, C. M. Kyaw, Archaeal S-layers: Overview and current state of the art. *Frontiers in Microbiology* **8**, 1–17 (2017).

8. M. Pohlschroder, F. Pfeiffer, S. Schulze, M. F. A. Halim, Archaeal cell surface biogenesis. *FEMS Microbiology Reviews* **42**, 694–717 (2018).

9. M. F. Abdul-Halim, *et al.*, Lipid Anchoring of Archaeosortase Substrates and Midcell Growth in Haloarchaea. *mBio* **11**, e00349-20 (2020).

10. M. F. Abdul Halim, *et al.*, Permuting the PGF Signature Motif Blocks both Archaeosortase-Dependent C-Terminal Cleavage and Prenyl Lipid Attachment for the Haloferax volcanii S-Layer Glycoprotein. *Journal of Bacteriology* **198**, 808–815 (2016).

11. H. Engelhardt, Are S-layers exoskeletons? The basic function of protein surface layers revisited. *Journal of Structural Biology* **160**, 115–124 (2007).

12. C. Zhang, *et al.*, Cell Structure Changes in the Hyperthermophilic Crenarchaeon Sulfolobus islandicus Lacking the S-Layer. *mBio* **10**, e01589-19 (2019).

13. C. Zhang, A. P. R. Phillips, R. L. Wipfler, G. J. Olsen, R. J. Whitaker, The essential genome of the crenarchaeal model Sulfolobus islandicus. *Nature Communications* **9**, 4908 (2018).

14. A. W. Bisson-Filho, J. Zheng, E. Garner, Archaeal imaging: leading the hunt for new discoveries. *Molecular biology of the cell* **29**, 1675–1681 (2018).

15. S. Schwarzer, M. Rodriguez-Franco, H. M. Oksanen, T. E. F. Quax, Growth Phase Dependent Cell Shape of Haloarcula. *Microorganisms* **9** (2021).

16. I. G. Duggin, *et al.*, CetZ tubulin-like proteins control archaeal cell shape. *Nature* **519**, 362–5 (2015).

17. Z. Li, *et al.*, Positioning of the Motility Machinery in Halophilic Archaea. *mBio* **10** (2019).

18. Y. Liao, S. Ithurbide, C. Evenhuis, J. Löwe, I. G. Duggin, Cell division in the archaeon Haloferax volcanii relies on two FtsZ proteins with distinct functions in division ring assembly and constriction. *Nat Microbiol* **6**, 594–605 (2021).

19. H. Schiller, *et al.*, Identification and characterization of structural and regulatory cell-shape determinants in Haloferax volcanii. 2023.03.05.531186 (2023).

20. C. Shi, *et al.*, Atomic-resolution structure of cytoskeletal bactofilin by solid-state NMR*. *Science Advances* **1**, e1501087 (2015).

21. S. Vasa, *et al.*, β-Helical architecture of cytoskeletal bactofilin filaments revealed by solid-state NMR. *Proceedings of the National Academy of Sciences* **112**, E127–E136 (2015).

22. J. Kühn, *et al.*, Bactofilins, a ubiquitous class of cytoskeletal proteins mediating polar localization of a cell wall synthase in Caulobacter crescentus. *The EMBO journal* **29**, 327–339 (2010).

23. X. Deng, *et al.*, The structure of bactofilin filaments reveals their mode of membrane binding and lack of polarity. *Nat Microbiol* **4**, 2357–2368 (2019).

24. J. E. Andari, F. Altegoer, G. Bange, P. L. Graumann, Bacillus subtilis Bactofilins Are Essential for Flagellar Hook- and Filament Assembly and Dynamically Localize into Structures of Less than 100 nm Diameter underneath the Cell Membrane. *PLOS ONE* **10**, e0141546 (2015).

25. P. D. Caccamo, M. Jacq, M. S. VanNieuwenhze, Y. V. Brun, A Division of Labor in the Recruitment and Topological Organization of a Bacterial Morphogenic Complex. *Curr Biol* **30**, 3908-3922.e4 (2020).

26. S. R. Sichel, B. P. Bratton, N. R. Salama, Distinct regions of H. pylori's bactofilin CcmA regulate protein–protein interactions to control helical cell shape. *eLife* **11**, e80111 (2022).

27. M. K. Koch, C. A. McHugh, E. Hoiczyk, BacM, an N-terminally processed bactofilin of Myxococcus xanthus, is crucial for proper cell shape. *Molecular Microbiology* **80**, 1031–1051 (2011).

28. M. R. Brockett, J. Lee, J. V. Cox, G. W. Liechti, S. P. Ouellette, A Dynamic, Ring-Forming Bactofilin Critical for Maintaining Cell Size in the Obligate Intracellular Bacterium Chlamydia trachomatis. *Infection and Immunity* **89** (2021).

29. S. Pöhl, *et al.*, A dynamic bactofilin cytoskeleton cooperates with an M23 endopeptidase to control bacterial morphogenesis. *eLife* **12** (2024).

30. L. Lin, M. Osorio Valeriano, A. Harms, L. Søgaard-Andersen, M. Thanbichler, Bactofilin-mediated organization of the ParABS chromosome segregation system in Myxococcus xanthus. *Nat Commun* **8**, 1817 (2017).

31. I. Bulyha, *et al.*, Two Small GTPases Act in Concert with the Bactofilin Cytoskeleton to Regulate Dynamic Bacterial Cell Polarity. *Developmental Cell* **25**, 119–131 (2013).

32. J. Jumper, *et al.*, Highly accurate protein structure prediction with AlphaFold. *Nature* **596**, 583–589 (2021).

33. R. Evans, *et al.*, Protein complex prediction with AlphaFold-Multimer. 2021.10.04.463034 (2022).

34. T. Frickey, A. Lupas, CLANS: a Java application for visualizing protein families based on pairwise similarity. *Bioinformatics* **20**, 3702–3704 (2004).

35. S. Holtrup, P. L. Graumann, Strain-dependent motility defects and suppression by a flhO mutation for B. subtilis bactofilins. *BMC Research Notes* **15**, 168 (2022).

36. J. Zheng, *et al.*, Salactin, a dynamically unstable actin homolog in Haloarchaea. *mBio* **14**, e02272-23 (2023).

37. D. A. Ball, *et al.*, Single molecule tracking of Ace1p in Saccharomyces cerevisiae defines a characteristic residence time for non-specific interactions of transcription factors with chromatin. *Nucleic Acids Research* **44**, e160 (2016).

38. A. Ranjan, *et al.*, Live-cell single particle imaging reveals the role of RNA polymerase II in histone H2A.Z eviction. *eLife* **9**, e55667 (2020).

39. A. von Kügelgen, V. Alva, T. A. M. Bharat, Complete atomic structure of a native archaeal cell surface. *Cell Reports* **37**, 110052 (2021).

40. J. A. Taylor, *et al.*, Distinct cytoskeletal proteins define zones of enhanced cell wall synthesis in Helicobacter pylori. *eLife* **9**, e52482 (2020).

41. T. Rados, K. Andre, M. Cerletti, A. Bisson, A sweet new set of inducible and constitutive promoters in Haloferax volcanii. *Front. Microbiol.* **14**, 1204876 (2023).

42. G. R. Squyres, *et al.*, Single-molecule imaging reveals that Z-ring condensation is essential for cell division in Bacillus subtilis. *Nat Microbiol* **6**, 553–562 (2021).

43. K. D. Whitley, *et al.*, FtsZ treadmilling is essential for Z-ring condensation and septal constriction initiation in Bacillus subtilis cell division. *Nat Commun* **12**, 2448 (2021).

44. A. B. Paaby, M. V. Rockman, The many faces of pleiotropy. *Trends Genet* **29**, 66–73 (2013).

45. F. Li, *et al.*, Pleiotropic cell-division defects and apoptosis induced by interference with survivin function. *Nat Cell Biol* **1**, 461–466 (1999).

46. F. Huber, *et al.*, Emergent complexity of the cytoskeleton: from single filaments to tissue. *Advances in Physics* **62**, 1–112 (2013).

47. D. A. Fletcher, R. D. Mullins, Cell mechanics and the cytoskeleton. *Nature* **463**, 485–492 (2010).

48. J. A. Theriot, Why are bacteria different from eukaryotes? *BMC biology* **11**, 119 (2013).

49. C. H. S. Aylett, J. Löwe, L. A. Amos, New insights into the mechanisms of cytomotive actin and tubulin filaments. *International review of cell and molecular biology* **292**, 1–71 (2011).

50. J. Lowe, L. A. Amos, Evolution of cytomotive filaments: the cytoskeleton from prokaryotes to eukaryotes. *Int J Biochem Cell Biol* **41**, 323–329 (2009).

51. A. Kareem, *et al.*, De novo assembly of plant body plan: a step ahead of Deadpool. *Regeneration (Oxf)* **3**, 182–197 (2016).

52. S. Hussain, *et al.*, MreB filaments align along greatest principal membrane curvature to orient cell wall synthesis. *eLife* **7**, e32471 (2018).

53. H. T. McMahon, J. L. Gallop, Membrane curvature and mechanisms of dynamic cell membrane remodelling. *Nature* **438**, 590–596 (2005).

54. A. Robert, C. Hookway, V. I. Gelfand, Intermediate filament dynamics: What we can see now and why it matters. *Bioessays* **38**, 232–243 (2016).

55. A. M. E. Baker, T. M. Roberts, M. Stewart, 2.6Å Resolution Crystal Structure of Helices of the Motile Major Sperm Protein (MSP) of Caenorhabditis elegans. *Journal of Molecular Biology* **319**, 491–499 (2002).

56. J. M. Wagstaff, *et al.*, A Polymerization-Associated Structural Switch in FtsZ That Enables Treadmilling of Model Filaments. *mBio* **8** (2017).

57. a Wegner, Head to tail polymerization of actin. *Journal of molecular biology* **108**, 139–50 (1976).

58. P. Nußbaum, *et al.*, An Oscillating MinD Protein Determines the Cellular Positioning of the Motility Machinery in Archaea. *Current Biology* **30**, 4956-4972.e4 (2020).

59. J. C. Walsh, *et al.*, Division plane placement in pleomorphic archaea is dynamically coupled to cell shape. *Molecular microbiology* **112**, 785–799 (2019).

60. C. D. A. Rodrigues, E. J. Harry, The Min System and Nucleoid Occlusion Are Not Required for Identifying the Division Site in Bacillus subtilis but Ensure Its Efficient Utilization. *PLOS Genetics* **8**, e1002561 (2012).

61. S. A. Flores, M. Howell, J. J. Daniel, R. Piccolo, P. J. B. Brown, Absence of the Min System Does Not Cause Major Cell Division Defects in Agrobacterium tumefaciens. *Front Microbiol* **9**, 681 (2018).

62. M. W. Bailey, P. Bisicchia, B. T. Warren, D. J. Sherratt, J. Männik, Evidence for Divisome Localization Mechanisms Independent of the Min System and SlmA in Escherichia coli. *PLOS Genetics* **10**, e1004504 (2014).

63. T. A. M. Bharat, A. von Kügelgen, V. Alva, Molecular Logic of Prokaryotic Surface Layer Structures. *Trends in Microbiology* **29**, 405–415 (2021).

Figure Legends

Figure 1. Halofilins comprise two large subgroups of structurally and evolutionarily diverse bactofilin homologs. (A) Cartoon representation of the predicted structure of HalA from *H. volcanii*. HalA is shown aligned to a TtBac filament (PDB entry 6RIA, chains from left to right: K, H, G, D). Side (left) and top (right) views are shown. MTS, membrane-targeting sequence. **(B)** Membrane positioning of the predicted structure of HalB from *H. volcanii*. The structure is lacking the signal peptide (see Methods). Side (left) and top (right) views are shown. **(C)** Cluster map of canonical bactofilins together with HalA and HalB. A set of 8,542 protein sequences is shown. Each dot represents one protein sequence, and each line represents pairwise similarity between two sequences, as calculated by BLASTp. The darker the line, the smaller the BLASTp E-value. Representative sequences are annotated for each cluster, and a cartoon representation of their predicted structure - except for TtBac, solved experimentally (PDB 6RIA-A) - is shown next to it. Each structure model shares the same color code as the legend. Clustering was achieved at an E-value cutoff of 1e-10, and edges in the map are shown for E-values ≤ 1e-8. Seed sequence and structure model accessions are provided in Tables S1 and S2.

Figure 2. HalA assembles into dynamic filaments and HalB as distinct foci in live cells. **(A)** Widefield fluorescence and phase contrast (left-column panels) and 3D-SoRa super-resolution (right-column panels) micrographs of cells expressing HalA-msfGFP (orange) and HalB-msfGFP (blue). Membranes of cells from 3D-SoRa images were stained with Nile Blue (grey). **(B)** Phase-contrast and epifluorescence microscopy time-lapses of HalA-msfGFP cells show a plethora of dynamic behaviors from HalA polymers, such as polarized elongation (top, first row) and depolymerization (second row), annealing between two filaments (third row) and filament fragmentation (bottom, fourth row). **(C)** Despite not showing evident dynamic instability, HalA depolymerization is still twice as fast as polymerization. **(D)** HalB assembles as slow-diffusing foci across the cell membrane. Unless specified, scale bars represent 5µm.

Figure 3. Experimental validation of HalA polymerization and HalB structural topology. (A) Cells coexpressing HalA-HaloTag together with different truncated versions of HalA. Depolymerization of HalA was extensive in most constructs but under the N-terminal subdomain alone (bottom-center panel). Cell outlines were drawn to support the identification of HalA polymers. **(B)** Cartoons representing the HalB-HaloTag fusions created by tagging HalB at its C-terminal (predicted cytoplasmic region, top panel) or next to its bactofilin subdomain (predicted extracellular region, bottom panel). **(C)** Cells expressing the HalB-HaloTag fusions were incubated simultaneously with 100 nM of HaloTag-ligand Alexa488 (left panels, green) and JF549 (right panels, blue) and imaged by phase contrast and epifluorescence microscopy. Unless specified, scale bars represent 5µm.

Figure 4. HalA and HalB specifically affect rods and disks. (A) 3D-SoRa projections of wild-type cells compared to *halA*, *halB*, and *halAB* deletion mutants. Cell membranes were labeled with Nile Blue. Arrowheads indicate an increasing scale of rod deformities from extremely bent and long cells (pink), bent but with average cell size (blue), and slightly bent at the cell poles (blue). **(B)** Cumulative distributions of rods (left) and disks (right) cell solidties from phase contrast images (Fig S7A). Dashed lines indicate the median values of the distribution. Kolmogorov-Smirnov tests were applied to pairs between wild type:Δ*halB* (rods), wild type:Δ*halA* (disks), resulting in statistically significant differences ($p<0.005$) for all pairs except for Δ*halA*: Δ*halAB* (rods), and Δ*halB*: Δ*halAB* (disks).

Figure 5. HalA and HalB play orthogonal membrane-remodeling roles in rods and disks. **(A)** Submicron mapping across halofilin mutants compared to their parental wild type shows specific but different dependence of HalA and HalB to prevent the emergence of extreme positive and negative curvatures. Representative cells were arbitrarily chosen, and their membrane curvature scale was labeled in red (negative), white (neutral), and blue (positive). **(B)** Cumulative distributions of each dataset's 25% extreme negative and positive Gaussian curvatures. Dashed lines indicate the median values ($\mu_{1/2}$) of the distribution. **(C)** Correlation between spatial localization of membrane curvatures and fluorescence intensity profile shows the affinity of HalA for positive (cytoplasmic surface) and HalB for negative (extracellular surface) membrane curvatures. **(D)** HalA overexpression completely vanishes rod-shaped cell populations while creating larger, deformed disks, while upregulation of *halB* also results in larger and mishappen disks but relatively standard rods.

Figure 6. *ΔhalA* and *ΔhalB* mutant cells show Z-ring decondensation but drastic morphological defects during shapeshift. (A) Localization of the cytokinetic Z-ring by labeling the tubulin homolog FtsZ2-msfGFP. **(B)** Normalized heatmaps of the relative localization of the FtsZ2-msfGFP intensity profiles across the major axis of rod cells in wild-type and mutant populations. **(C)** Correlation between relative Z-ring position and cell area suggests a bias to cell division misplacement in larger, deformed cells. **(D)** Single cell tracking of cell solidity plotted against normalized cytokinesis periods depicting the deformation profile of cells during cell division. A Lorentzian function was used to fit the deformations (constriction) and relief (separation) events from the wild-type (29 cells), Δ*halA* (31 cells), and Δ*halB* (28 cells) strains. **(E)** Single-cell tracking of cell solidities plotted against a normalized cell cycle period depicting the deformation profile of non-transitioning cell elongation during a single doubling-time growth period. The average trace across all data points was used to fit the deformations (disk-rod transition) and relief (rod-cell elongation) events from the wild-type (32 cells), Δ*halA* (36 cells), and Δ*halB* (29 cells) strains. **(F)** Single-cell tracking of cell solidities plotted against normalized shapeshift periods depicting the deformation of cells during disk-rod transitions. A Lorentzian function was used to fit the deformations (disk-rod transition) and relief (rod-cell elongation) events from the wild-type (40 cells), Δ*halA* (41 cells), and Δ*halB* (38 cells) strains. **(G)** Representative examples of cells shapeshifting from disks to rods throughout approximately a quarter of the cell cycle period. Scale bars represent 5µm.

Figure 7. Proposed model for how HalA and HalB act at different time points during disk-rod shape transitions. (A) Summary of shape transition stages at the cellular scale level. Disks sense the (still unknown) signal from the environment and trigger the shape-shift developmental program toward rod cells. Cell division resumes after the shape transition is finalized. The division site (Z-ring) is represented in yellow. **(B)** Zoom-in of the proposed molecular mechanism of HalA (pink) and HalB (blue) roles during shape transition. The dark grey outline represents the cytoplasmic membrane and the S-layer lattice altogether. The upper envelope layer represents the process in wild-type cells, while the bottom flow illustrates the scenarios in the Δ*halA* and Δ*halB* strains. Z-ring yellow threads represent FtsZ1 and FtsZ2 protofilaments.

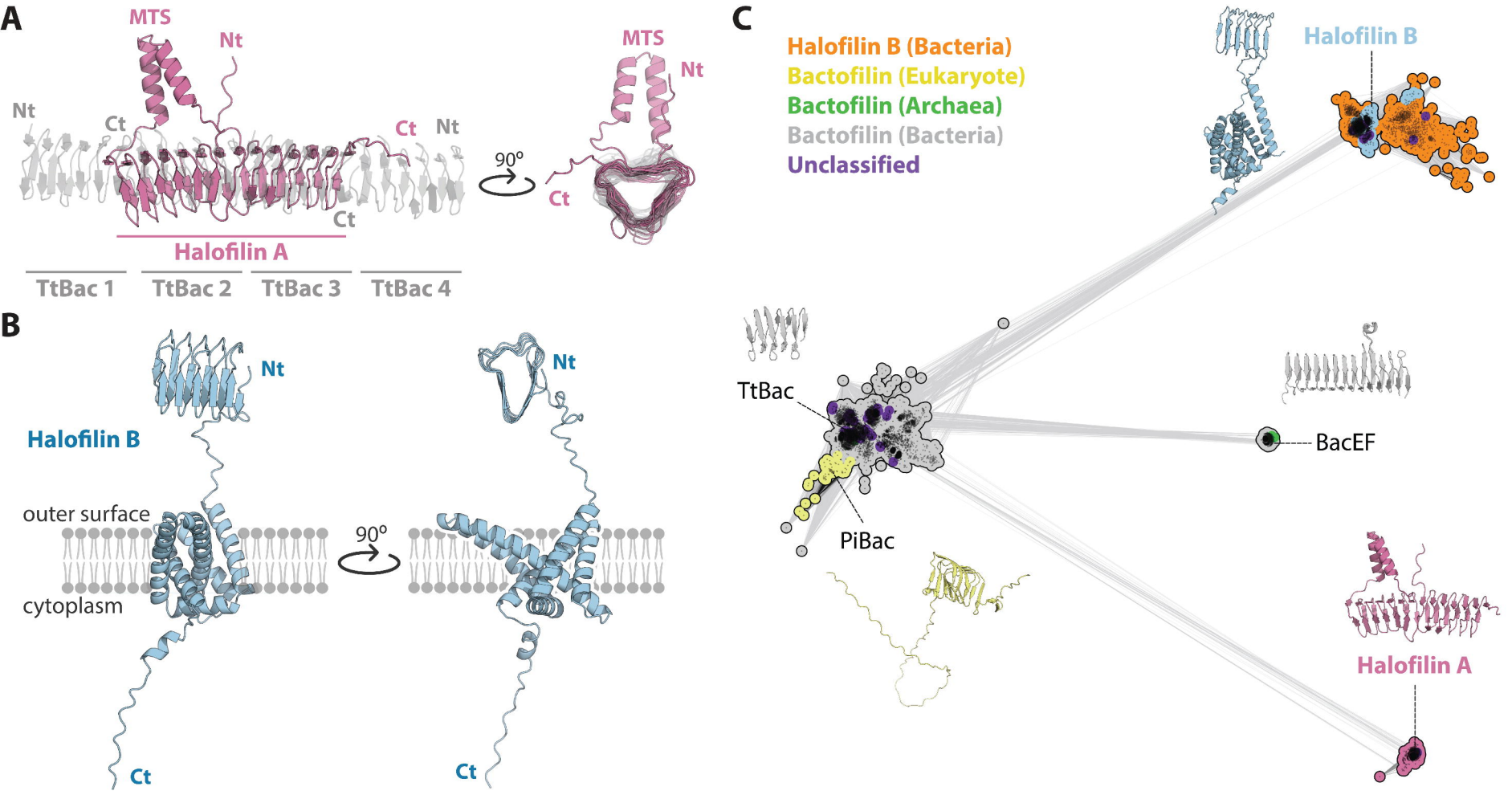
A
MTS
Nt
Nt
Ct
Ct
Nt
Ct
Halofilin A
TtBac 1
TtBac 2
TtBac 3
TtBac 4
90°
MTS
Nt
Ct
B
Nt
Halofilin B
outer surface
cytoplasm
Ct
90°
Nt
Ct
C
Halofilin B (Bacteria)
Bactofilin (Eukaryote)
Bactofilin (Archaea)
Bactofilin (Bacteria)
Unclassified
Halofilin B
TtBac
BacEF
PiBac
Halofilin A

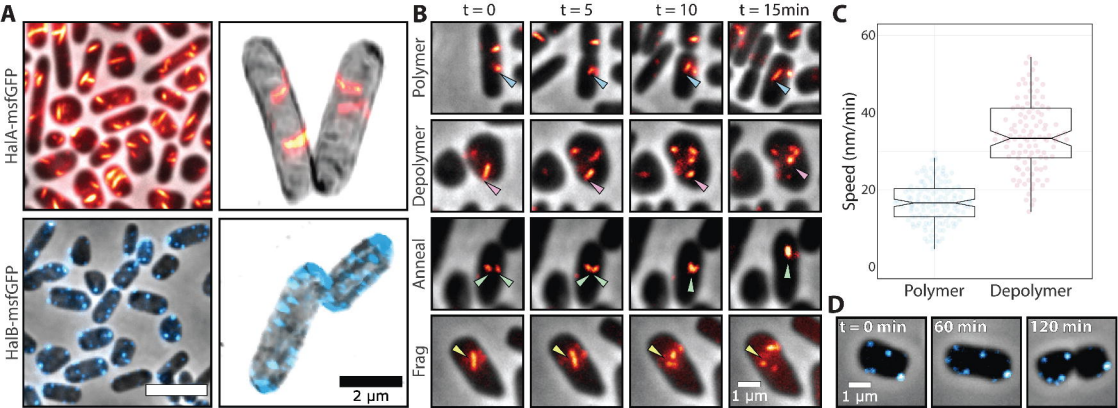
A
HalA-msfGFP
HalB-msfGFP
2 µm
B
t = 0
t = 5
t = 10
t = 15min
Polymer
Depolymer
Anneal
Frag
1 µm
C
Speed (nm/min)
60
40
20
0
Polymer
Depolymer
D
t = 0 min
60 min
120 min
1 µm

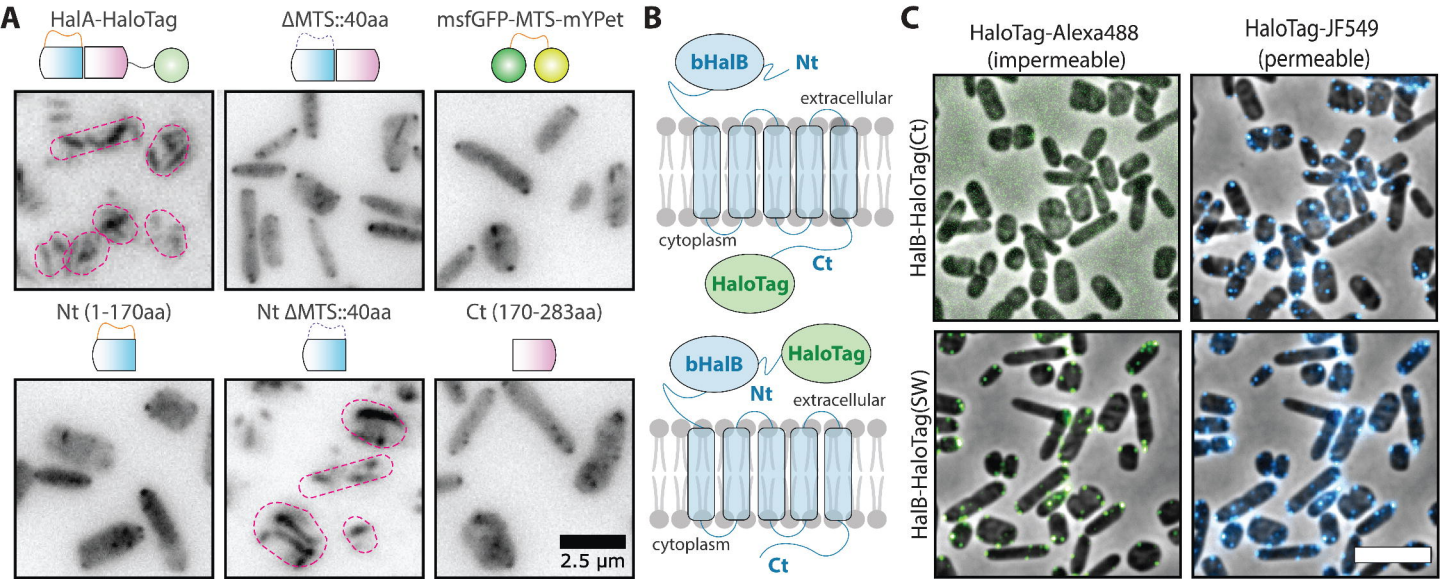
A
HalA-HaloTag
ΔMTS::40aa
msfGFP-MTS-mYPet
Nt (1-170aa)
Nt ΔMTS::40aa
Ct (170-283aa)
2.5 μm
B
bHalB
Nt
extracellular
cytoplasm
Ct
HaloTag
bHalB
HaloTag
Nt
extracellular
cytoplasm
Ct
C
HaloTag-Alexa488
(impermeable)
HaloTag-JF549
(permeable)
HalB-HaloTag(Ct)
HalB-HaloTag(SW)

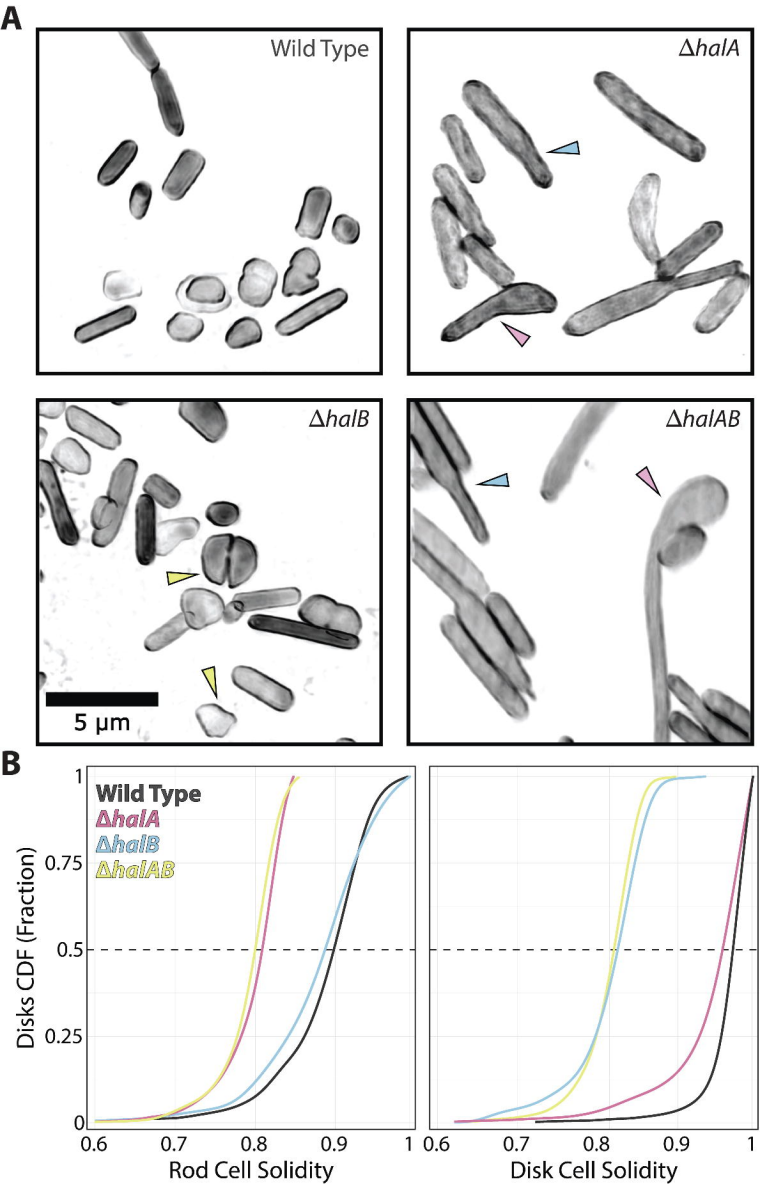
A
Wild Type
ΔhalA
ΔhalB
ΔhalAB
5 µm
B
Wild Type
ΔhalA
ΔhalB
ΔhalAB
Disks CDF (Fraction)
0
0.25
0.5
0.75
1
0.6
0.7
0.8
0.9
1
Rod Cell Solidity
Disk Cell Solidity

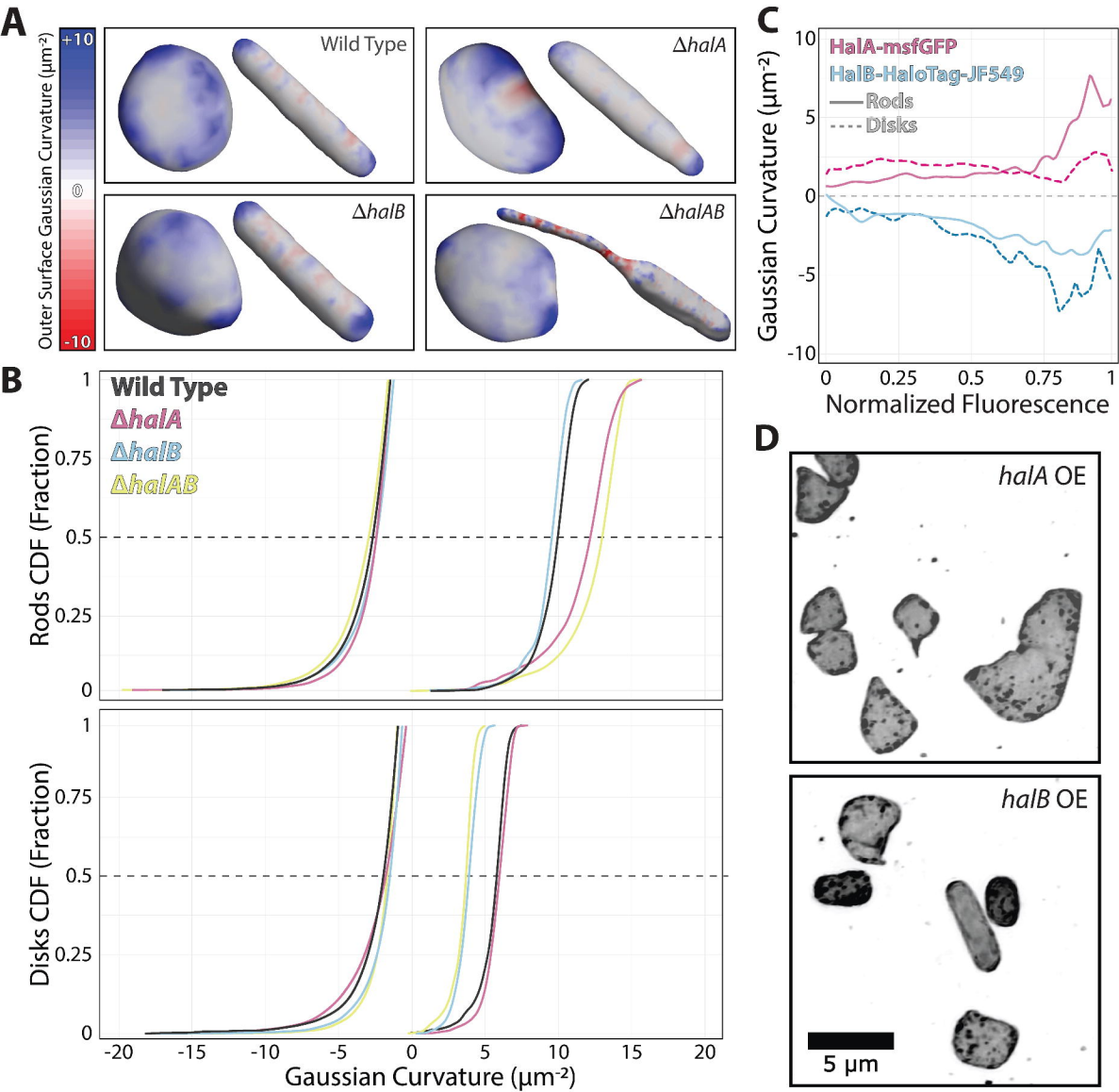
A
Outer Surface Gaussian Curvature (μm⁻²)
+10
0
-10
Wild Type
ΔhalA
ΔhalB
ΔhalAB
B
Wild Type
ΔhalA
ΔhalB
ΔhalAB
Rods CDF (Fraction)
Disks CDF (Fraction)
0
0.25
0.5
0.75
1
-20
-15
-10
-5
0
5
10
15
20
Gaussian Curvature (μm⁻²)
C
HalA-msfGFP
HalB-HaloTag-JF549
Rods
Disks
Gaussian Curvature (μm⁻²)
10
5
0
-5
-10
0
0.25
0.5
0.75
1
Normalized Fluorescence
D
halA OE
halB OE
5 μm

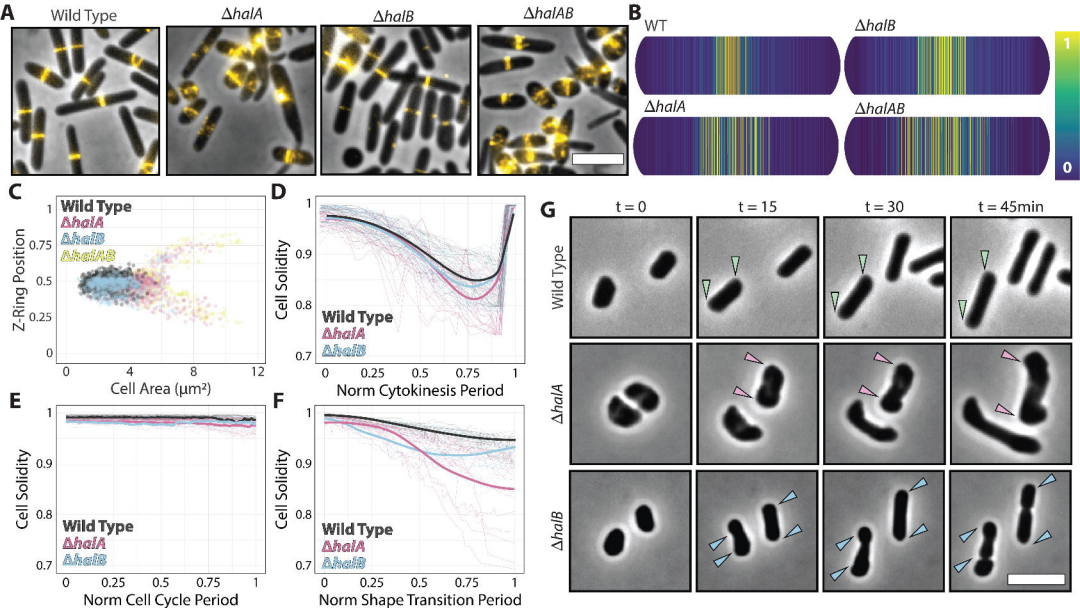
A
Wild Type
ΔhalA
ΔhalB
ΔhalAB
B
WT
ΔhalB
ΔhalA
ΔhalAB
1
0
C
Wild Type
ΔhalA
ΔhalB
ΔhalAB
Z-Ring Position
Cell Area (μm²)
D
Cell Solidity
Norm Cytokinesis Period
E
Cell Solidity
Norm Cell Cycle Period
F
Cell Solidity
Norm Shape Transition Period
G
t = 0
t = 15
t = 30
t = 45min
Wild Type
ΔhalA
ΔhalB

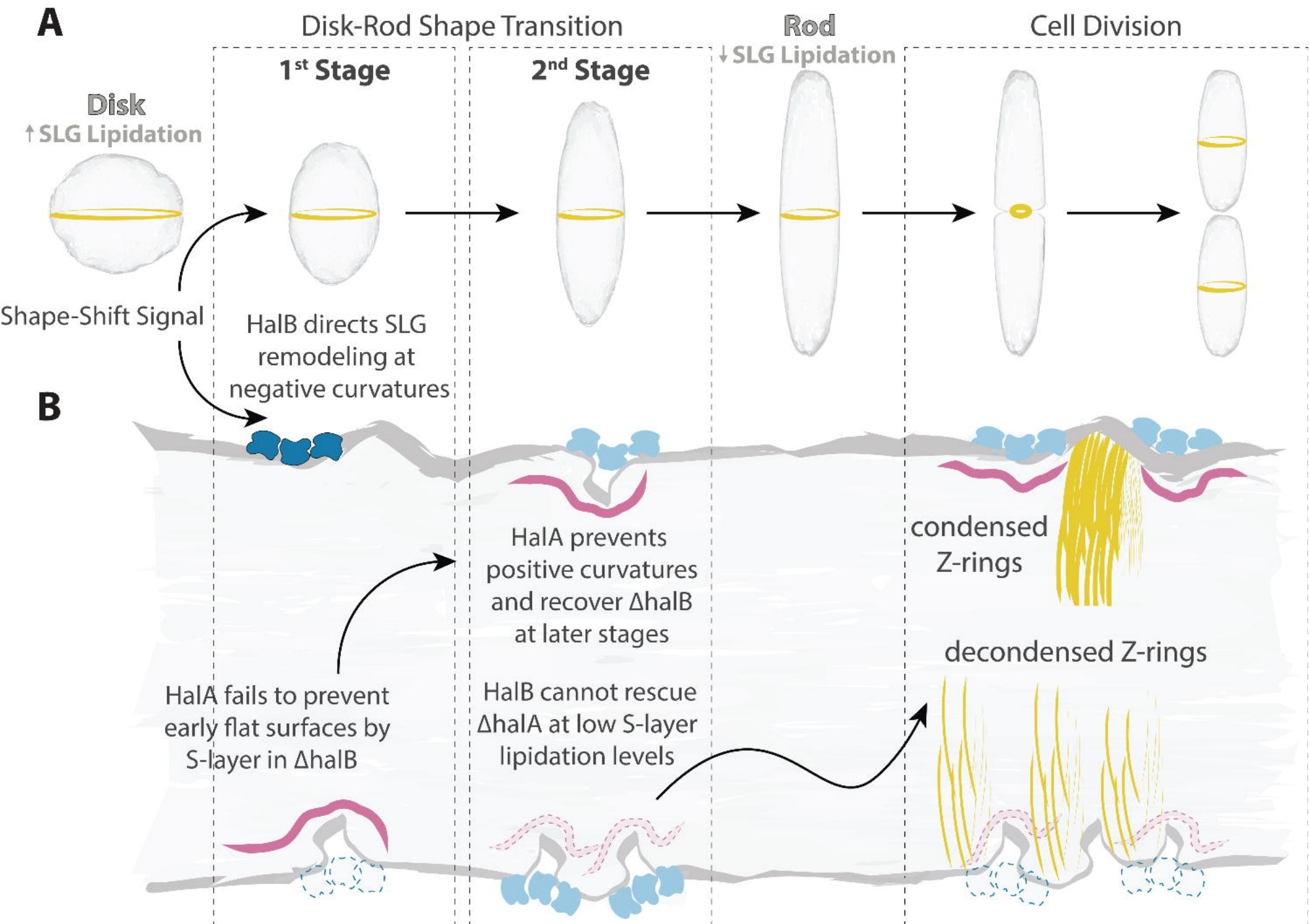
A
Disk-Rod Shape Transition
Rod
↓ SLG Lipidation
Cell Division
1st Stage
2nd Stage
Disk
↑ SLG Lipidation
Shape-Shift Signal
HalB directs SLG remodeling at negative curvatures
B
HalA prevents positive curvatures and recover ΔhalB at later stages
condensed Z-rings
decondensed Z-rings
HalA fails to prevent early flat surfaces by S-layer in ΔhalB
HalB cannot rescue ΔhalA at low S-layer lipidation levels